

## Chapter 4: Methods for *in-situ* microscopy

This chapter describes different methods for imaging quantum gases *in-situ* with modest spatial resolution and optimal signal-to-noise ratio (SNR). I describe basic imaging systems in the context of scalar diffraction, followed by the relevant aspects of light-matter interaction giving rise to the recorded intensity signals. I then present a number of practical calibration methods including magnification, spatial resolution, and saturation intensity. I end with a detailed analysis of image processing methods, from estimating uncertainties to implementing linear reconstruction algorithms that improve our SNR.

This chapter is organized as follows. In the first section 4.1, I introduce basic considerations for imaging quantum gases, beginning with scalar diffraction theory and a survey of basic imaging systems in 4.1.1, followed by the semiclassical framework of light-matter interaction in 4.1.2. Later, in section 4.2, I present a few experimental calibrations for optimized imaging, beginning with magnification in 4.2.1, spatial resolution in 4.2.2, and saturation intensity in 4.2.3. Finally, in section 4.3, I end the chapter with a description of image uncertainty estimation and propagation in 4.3.1, ideal and realistic

signal-to-noise ratio from resonant absorption bright-field microscopy in 4.3.2, and a detailed account of image reconstruction algorithms in 4.3.3.

## 4.1 Microscopy of two-level atoms

In the context of imaging, we may treat a quantum gas as a collection of atom-sized dipole antennas. Under this powerful abstraction, near-resonant optical fields couple with atomic ensembles, and relay information by absorbing, re-emitting, or shifting the phase of the incident light. The core task in the experiments presented in this thesis is microscopy, or the optimal retrieval of optical information emanating from microscopic systems.

### 4.1.1 Diffraction and the angular spectrum

A linearly polarized, monochromatic, and time-harmonic complex optical field satisfies the scalar Helmholtz equation

$$[\nabla^2 + k_0^2(1 + \chi(\vec{r}))]E(\vec{r}) = 0 \quad (4.1)$$

as it propagates through an inhomogeneous medium with complex electric susceptibility  $\chi(\vec{r})$ , and where  $k_0 = \omega_0/c$ , the free-space dispersion relation in terms of the angular frequency  $\omega_0$  and the speed of light  $c$ . It is possible to separate the Helmholtz equation

$$[\nabla_{\perp}^2 + k_0^2]E(\vec{r}) + k_0^2\chi(\vec{r})E(\vec{r}) + \frac{\partial^2 E(\vec{r})}{\partial z^2} = 0, \quad (4.2)$$

in the transverse and longitudinal differential operators. This equation can be formally integrated in  $z$  for a known field

$$E(\vec{r} + \delta z \mathbf{e}_z) = \exp \left[ \pm i \delta z \sqrt{\nabla_{\perp}^2 + k_0^2(1 + \chi(\vec{r}))} \right] E(\vec{r}) \quad (4.3)$$

propagating by  $\pm \delta z$  along  $\mathbf{e}_z$ . A convenient representation of the transverse optical field is the angular spectrum

$$\tilde{E}(k_x, k_y; z) = \hat{\mathcal{F}}[E(\vec{r})] = \frac{1}{4\pi^2} \iint_{-\infty}^{\infty} E(x, y; z) e^{-i(k_x x + k_y y)} dx dy, \quad (4.4)$$

in terms of a plane-wave decomposition. The angular spectrum  $\tilde{E}(k_x, k_y; z)$  in the transverse spatial frequency space  $(k_x, k_y)$  forms a Fourier transform pair with the optical field  $E(x, y; z)$  in the coordinate space  $(x, y)$ , located at  $z$ . The angular spectrum transforms to

$$E(k_x, k_y; z \pm \delta z) = E(k_x, k_y; z) e^{\pm i k_z \delta z} \quad (4.5)$$

under a displacement  $\pm \delta z$  in free space propagation. Meanwhile, the longitudinal wavenumber

$$k_z^2 = k_0^2(1 + \chi_0) - k_x^2 - k_y^2$$

sets a spatial frequency cutoff for evanescent ( $k_z^2 < 0$ ), stationary ( $k_z^2 = 0$ ), and propagating ( $k_z^2 > 0$ ) modes in the homogeneous medium with susceptibility  $\chi_0$ . In vacuum (or air), Equation 4.5 becomes the formal solution in Equation

4.3 for  $\chi(\vec{r}) = 0$ , as in Fourier space the transverse operator transforms to  $\hat{\mathcal{F}}[\nabla_\perp] = ik_\perp$ . When passing through an aperture described by the function  $\mathcal{A}(x, y)$ , the angular spectrum transforms according to

$$\tilde{E}_+(k_x, k_y; z \pm \delta z) = \hat{\mathcal{F}}[E_-(x, y, z)\mathcal{A}(x, y)]. \quad (4.6)$$

Similarly, upon propagating through a thin lens, the field giving rise to the angular spectrum

$$\tilde{E}_+(k_x, k_y; z) = \hat{\mathcal{F}}[E_-(x, y; z)e^{\frac{ik_0}{2f}(x^2+y^2)}] \quad (4.7)$$

acquires a quadratic phase factor adding a constant curvature scaled by the focal length  $f$  to the wavefront. In the previous two situations, the different components of the angular spectrum  $\tilde{E}_+$  evolve according to 4.5 if propagating through free space. One of the key insights of the angular spectrum representation is that most imaging systems act as effective low pass filters for the incident angular spectra. The high-frequency cutoff gives an approximate diffraction-limited spatial resolution

$$\Delta \approx \frac{0.61\lambda}{\text{NA}}, \quad (4.8)$$

related to the largest transverse wavenumber  $k_{\text{NA}} = \pi/\Delta$  entering the numerical aperture NA. The Rayleigh's criterion is valid for small apertures where the incident ray angles satisfy  $\sin \theta_{\text{NA}} \approx \theta_{\text{NA}}$ , an insight first provided by Abbe

in 1867 [54]. In this limit, a lateral translation degrading the spatial resolution by more than  $\sim 20\%$  sets the field of view. Longitudinal translations preserve the transverse spatial resolution within a depth of field

$$\zeta = \frac{\lambda}{\text{NA}^2}. \quad (4.9)$$

While maximizing the numerical aperture gives finer spatial resolution, the depth of field decreases more rapidly.

#### 4.1.2 Imaging systems

An imaging system is the collection of optical elements that map optical fields into other planes along their propagation. Since detection is typically carried out in a two-dimensional plane, an imaging system transforms the transverse optical field from an object plane to the detection, or imaging plane. Different elements of an imaging system perform close to linear transformations on the propagating optical fields. The following examples of imaging systems are intended for the advanced undergraduate or graduate student starting the design of a simple imaging system.

A lensless imaging system may contain flat mirrors, and apertures, but no lenses or other curved surfaces. Lensless imaging systems have no magnifying effect on the objects encoded by the optical field distributions. Since the intensity decays as  $z_i^2$ , measuring the squared distance from the object plane,

while an image can be projected arbitrarily far along propagation, recording it may prove difficult in practice. Nevertheless, lensless microscopy offers reduced aberrations around the optical axis.

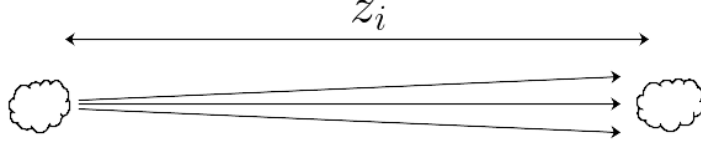


Figure 4.1: Schematic drawing of a lensless imaging system. The distance from the object to the image is  $z_i$ .

A single lens imaging system may contain mirrors, apertures and one lens. Single lens microscopes are practical for either very large or very small values of the magnification, especially in applications with constrained longitudinal space. A single (thin) lens imaging system produces images in different planes according to the lens-maker equation

$$\frac{1}{z_o} + \frac{1}{z_i} = \frac{1}{f}, \quad (4.10)$$

with magnification

$$M = -\frac{z_o}{z_i} \quad (4.11)$$

equal to the ratio of the distances from the lens to the object  $z_o$  and to the image  $z_i$ . The negative sign signifies a vertical inversion with respect to the orientation of the object. As an example, to demagnify an object by a factor of  $1/3$ , equation 4.11 relates the distances from object to image as  $3z_o = z_i$ . Then, picking a  $f = 100$  mm singlet to realize this gives the values  $z_o = 133.33$  mm

and  $z_i = 400$  mm through 4.10. In single lens imaging systems, when the object is placed at  $z_o < f$  it forms a virtual image, i.e. with no projection.

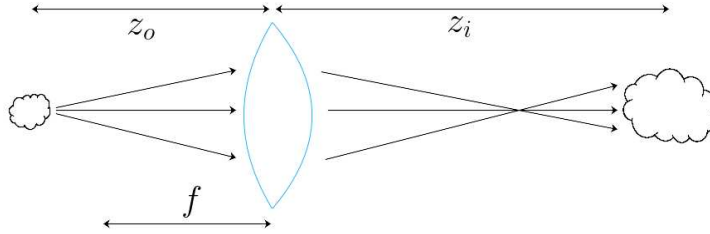


Figure 4.2: Schematic drawing of a single lens imaging system. The distance from the object to the lens is  $z_o$ , while the distance from the lens to the image is  $z_i$ . The lens has focal length  $f$ .

A two lens imaging system may contain mirrors, apertures, and two lenses. Two lens microscopes are a popular choice as they conjugate optical fields giving access to Fourier planes where the modulus squared angular spectra become diagonal in real space (i.e. the intensity Fourier transform). We can work out the effect of a two lens imaging system by chaining two single lens imaging systems. The distance from the object to the first (objective) lens with focal length  $f_1$  is  $z_o$ , forming an image in

$$z_1^{-1} = f_1^{-1} - z_o^{-1} \quad (4.12)$$

with magnification  $M_1 = -z_o/z_1$ . Then, a second (eyepiece) lens with focal length  $f_2$ , at a distance  $z_2$  behind  $z_1$  forms an image in

$$z_i^{-1} = f_2^{-1} - z_2^{-1} \quad (4.13)$$

with additional magnification  $M_2 = -z_2/z_i$ . The total magnification becomes  $M = M_1 M_2$ . An interesting case arises when  $z_o = f_1$ , and  $z_i = f_2$ . There, the object going through the first lens forms an image at infinity which the second lens picks to form an image a distance  $f_2$ . The net effect is to conjugate the object by a total distance of  $2f_1 + 2f_2$ , forming an image approximately 4 focal distances away. This special case comprises a  $4f$ -system, with total magnification  $M = -f_2/f_1$  given by the ratio of the focal lengths. As an

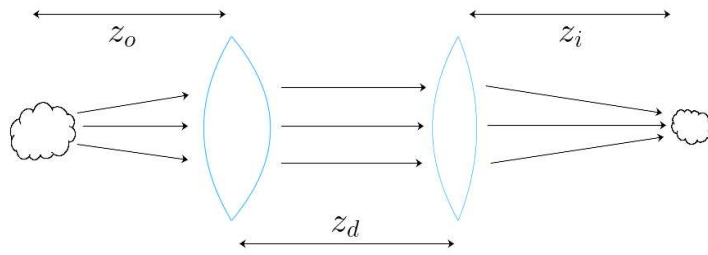


Figure 4.3: Schematic of a two lens imaging system. The ray diagram corresponds to the path traveled by light in the  $4f$  configuration, where the object is conjugated to an image  $2f_1 + 2f_2$  away. The distance between the lenses  $z_d = f_1 + f_2$ .

example, to magnify an object by  $M = 8$  using a two lens imaging system, using an  $f_1 = 40$  mm objective lens, we need to place an  $f_2 = 320$  mm eyepiece a distance  $z_d = 360$  mm behind the objective.

### 4.1.3 Light-matter interaction

The theory of scalar atom-light interaction describes how near-resonant light induces an electric dipole on the atom, which then scatters the light field. Several frameworks capture this interaction for a two-level system, including



the minimal set of optical Bloch equations [55]

$$\begin{aligned}
\dot{\rho}_{ee} &= i\frac{\hbar\Omega}{2}(\rho_{eg} - \rho_{ge}) - \hbar\Gamma\rho_{ee} \\
\dot{\rho}_{gg} &= -i\frac{\hbar\Omega}{2}(\rho_{eg} - \rho_{ge}) + \hbar\Gamma\rho_{ee} \\
\dot{\rho}_{ge} &= -\left(i\hbar\delta + \frac{\hbar\Gamma}{2}\right)\rho_{ge} - i\frac{\hbar\Omega}{2}(\rho_{ee} - \rho_{gg}) \\
\dot{\rho}_{eg} &= \left(i\hbar\delta - \frac{\hbar\Gamma}{2}\right)\rho_{eg} + i\frac{\hbar\Omega}{2}(\rho_{ee} - \rho_{gg})
\end{aligned}$$

describing the evolution of the driven system with coupling strength  $\Omega$ , single field detuning  $\delta$ , and damping  $\Gamma$  capturing the spontaneous emission from the excited state. The optical Bloch equations account for the evolution of ground  $|g\rangle$ , and excited  $|e\rangle$  state populations through the matrix elements  $\hat{\rho}_{gg} = |g\rangle\langle g|$  and  $\hat{\rho}_{ee} = |e\rangle\langle e|$ , as well as the atomic state coherences in  $\hat{\rho}_{eg} = \hat{\rho}_{ge}^*$ . The steady state solution obtained by setting  $\dot{\hat{\rho}} = 0$  in the optical Bloch system above gives the excited state population

$$\rho_{ee}^{ss} = \frac{\Omega^2}{2\Gamma^2} \frac{1}{1 + \frac{\delta^2}{\Gamma^2} + \frac{\Omega^2}{\Gamma^2}} \quad (4.14)$$

from which the unitarity of  $\hat{\rho}$  gives  $\rho_{gg} = 1 - \rho_{ee}$ . Similarly, the steady-state coherence is

$$\rho_{eg}^{ss} = -i\frac{\Omega}{2\Gamma} \frac{1 + i\frac{\delta}{\Gamma}}{1 + \frac{\delta^2}{\Gamma^2} + \frac{\Omega^2}{\Gamma^2}}, \quad (4.15)$$

from which the hermiticity of  $\hat{\rho}$  gives  $\rho_{eg} = \rho_{ge}^*$ . In a macroscopic atomic ensemble, scattering of a near-resonant field causes intensity attenuation along

its propagation

$$\frac{dI}{dz} = -\sigma_0 n I \quad (4.16)$$

proportional to the density of the medium [55]. Microscopically, the density-matrix coherence gives the complex, linear electric susceptibility

$$\chi(\vec{r}, \delta) \propto \rho_{ge}^{ss}(\Omega, \Gamma, \delta) n(\vec{r}) = \frac{\sigma_0}{k_0} \frac{i - \bar{\delta}}{1 + s_0 + \bar{\delta}^2} n(\vec{r}) \quad (4.17)$$

governing light propagation through the atomic medium, and optical properties such as absorption, and phase shifts proportional to the atomic density distribution  $n(\vec{r})$ . The susceptibility in Equation 4.17 is in terms of the saturation parameter  $s_0 = 2\Omega^2/\Gamma^2$ , reduced detuning  $\bar{\delta} = 2\delta/\Gamma$ , driving field wavenumber  $k_0 = 2\pi/\lambda$ , and resonant atomic cross section  $\sigma_0 = 3\lambda^2/2\pi$ . Figure 4.4 illustrates the near-resonant absorption and phase-shift of a homogeneous cloud.

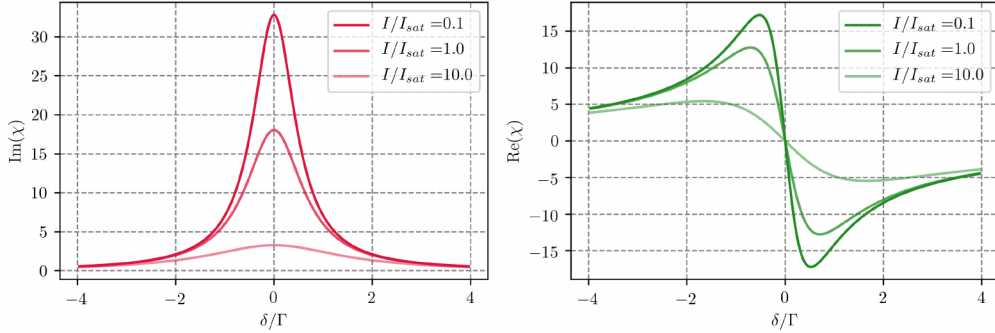


Figure 4.4: Real and imaginary parts of the two-level atomic susceptibility from Equation 4.17. The power broadening is evident for the three curves as a function of different saturation parameters. The parameters used in this calculation are  $\Gamma = 2\pi \times 6.06$  MHz,  $\lambda = 780.24$  nm,  $I_{\text{sat}} = 1.67$  mW/cm<sup>2</sup>, and a peak density of  $n_0 = 10^{15}$  cm<sup>-3</sup> for <sup>87</sup>Rb.

## 4.2 Calibration methods for imaging systems

### 4.2.1 Magnification

We calibrate the magnification of imaging systems using two different methods. One method uses a testbench and the other uses the atoms.

We place in the first method a calibrated **USAF-1951** test target with sets vertical and horizontal stripes sampling spatial frequencies down to  $0.228 \mu\text{m}^{-1}$  ( $\Delta x_{\min} = 4.38 \mu\text{m}$ ). After setting up an imaging system, we first image the back illuminated **USAF-1951** test target in focus, shown in Figure 4.5. Then, we take the cross-sectional intensity across multiple line pairs, or elements labeled by  $e$ , belonging to a same group  $g$ . Finally, we find the line edges and compute the distances between them. The spatial frequencies

$$k_{lp} = 2^{g+(e-1)/6} \quad (4.18)$$

(in line-pairs per mm) for group  $g$  and elements  $e$ , allow us to back out as many values of the magnification as the number of sampled group elements. The magnification may vary across the field-of-view due to resolution effects and/or uncertainty in line edge location, and we therefore take the mean magnification out of a single group when the variance is not too large. As an example, Figure 4.5 shows the calibrated magnification of  $\langle M \rangle = 4.03(4)$  of a two-lens

imaging system with  $f_2 = 150$  mm, and  $f_1 = 34.3$  mm, where the expected magnification is  $M_{exp} = 4.37$ .

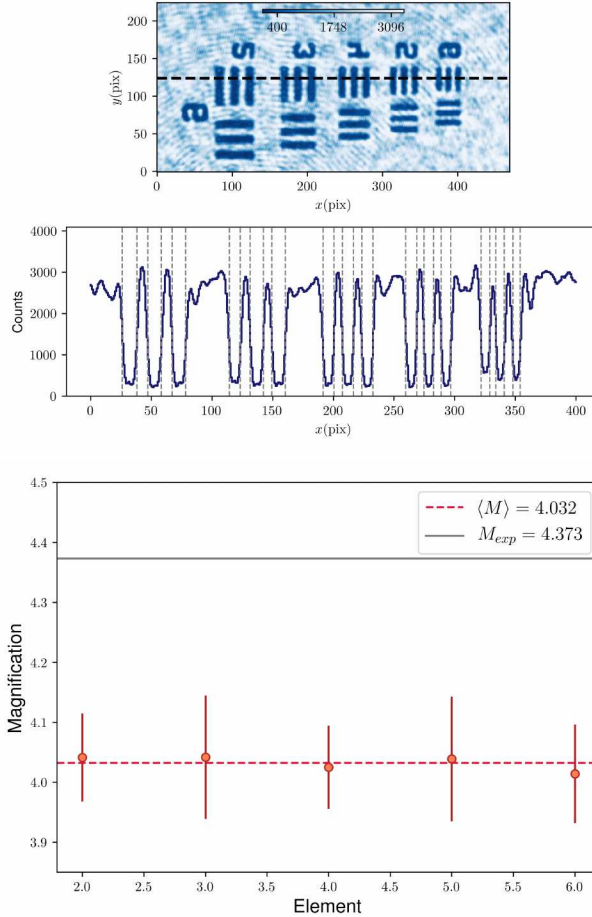


Figure 4.5: Calibrated magnification using a USAF-1951 test target. The test target pattern image (transmitted intensity in counts) at the top left effectively samples calibrated spatial frequencies. Below, a horizontal cross-section (dark blue) gives the distances in pixels between consecutive pairs of lines (dashed gray). We back out the magnification from 5 different group elements (red circles) and take the mean across the different elements (dashed red line). Errors in the two-lens locations and focal lengths propagate into the measured magnification  $M = 4.03(11)$ , different from the expected two-lens magnification (solid gray line) by  $\approx 8\%$ .

In the second method we scan the time-of-flight (TOF) of a falling cloud of atoms and measure its position as a function of time. The trajectory on the

detector

$$y_d(t) = M \left( y_0 + v_0 t + \frac{1}{2} g t^2 \right), \quad (4.19)$$

is magnified by a factor  $M$ . We fit the trajectory of the cloud to a scaled parabola and back out the magnification as a free parameter (assuming  $g = 9.81 \text{ m/s}^2$ ).

It is desirable to do this experiment using an  $|m_F = 0\rangle$  cloud as it is oblivious to stray magnetic field gradients that may change its trajectory. Figure 4.12 shows an example of this calibration method for a different imaging system,

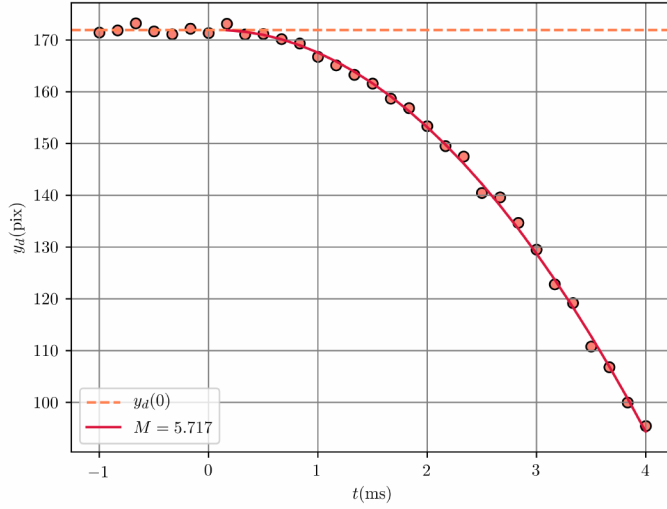


Figure 4.6: Calibrated magnification using a freely falling cloud of atoms. The vertical trajectory is monitored from  $t = -1 \text{ ms}$ , before the cloud is released in free fall, to  $t = 4 \text{ ms}$  after. The fit parabolic trajectory (solid red) spanning  $t > 0$  gives the magnified trajectory, from which  $M = 5.717(70)$ .

## 4.2.2 Spatial resolution

We only calibrate the spatial resolution of an imaging system directly on a test bench setup. By using circular apertures with radius  $a \ll \Delta x$ , much

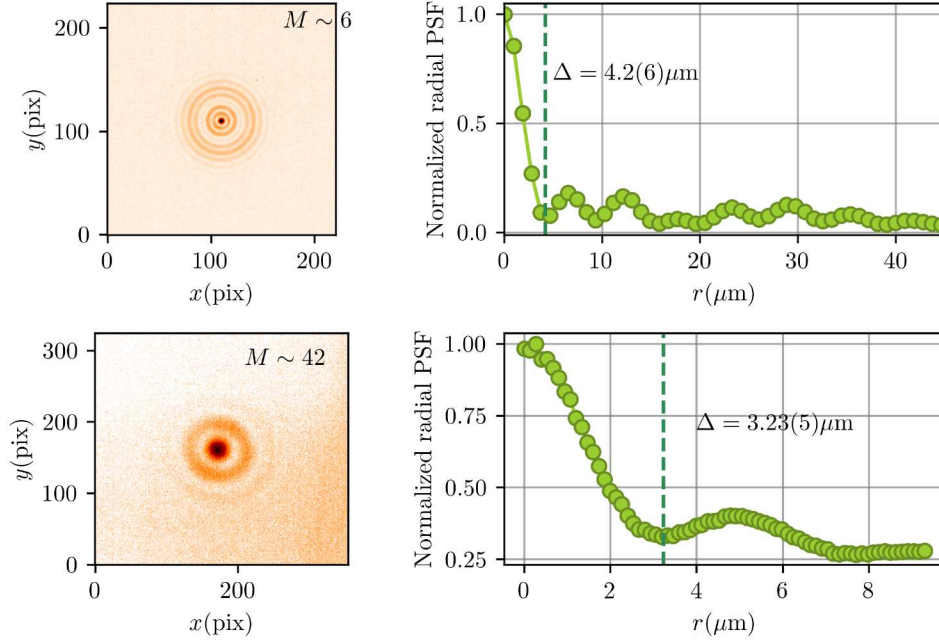


Figure 4.7: Calibrated resolutions using point spread function intensity. Two different imaging systems sample a  $1\text{ }\mu\text{m}$  pinhole with calibrated magnifications (top right annotation on the left column). The two systems produce different diffraction patterns from which effective spatial resolutions are  $\Delta = 4.2\text{ }\mu\text{m}$  (top), and  $\Delta = 3.2\text{ }\mu\text{m}$  (bottom). While a larger magnification gives a larger sampling rate and a more precise calibration, the signal-to-noise ratio is worse under a similar exposure.

smaller than the expected diffraction-limited resolution of the imaging system, we produce an Airy pattern on the image plane. For most  $\lambda = 780\text{ nm}$  illumination microscopes, a  $a = 1\text{ }\mu\text{m}$  pinhole is sufficient. Two example intensity patterns are in Figure 4.7, corresponding to a cut of the three-dimensional point-spread-function (PSF) of two different imaging systems. We take the effective spatial resolution as the distance from the peak to the first minimum of the Airy pattern.

### 4.2.3 Saturation intensity

We probe our atomic ensembles with resonant Gaussian beams. In spite of their inhomogeneous intensity distribution with respect to the cloud, an important calibration for the absorption profile of an atomic density distribution is  $I_{sat}$ , the saturation intensity in counts per pixel. Here, we present five different methods to calibrate the saturation intensity parameter. Since each  $I_{sat}$  calibration depends on the magnification of the imaging system, the examples below represent different instances of our *in-situ* imaging system and need not converge to a single value. Nevertheless, they may be combined simultaneously for reduced uncertainty and systematics if we understand the reason for their differences.

First is the beam profiling method, combining the intensity of a probe beam and a measurement of its power, assuming that the uncalibrated counts from the intensity profile match the measured power

$$P_0 = \sum_i I_i \Delta^2$$

where  $I_i$  is the intensity at pixel  $i$  and  $\Delta$  is the pixel size. As an example of this method, we measure  $P_0 = 23.3(2) \mu\text{W}$  in the probe from Figure 4.8 without taking into account any sensitivity or gain variations right after the objective lens, but estimate  $P_0 \approx 25.3 \mu\text{W}$  at the location of the atoms after

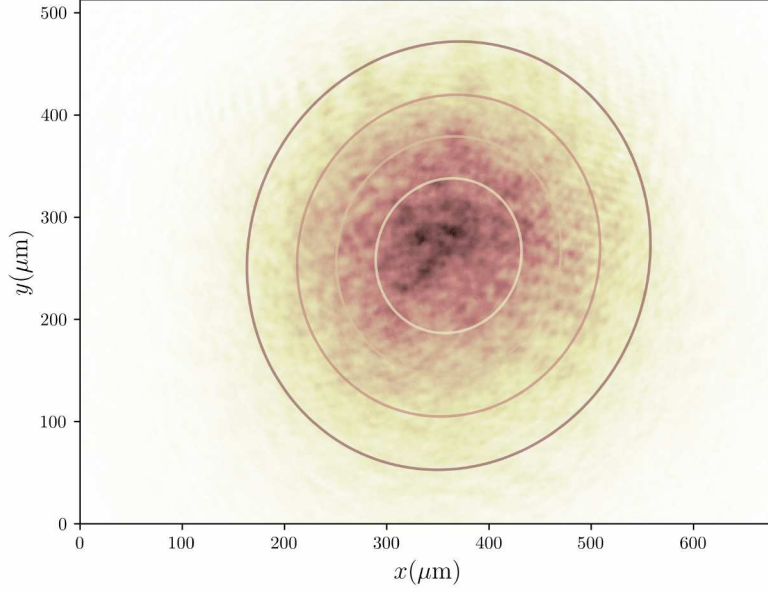


Figure 4.8: Raw probe intensity profile and Gaussian fit contours outlining  $\sigma$ ,  $2\sigma$ ,  $3\sigma$ , and  $4\sigma$  away from the center. The two-dimensional Gaussian fit gives a peak  $I_m = 1966$  counts, and major waists  $w_u = 103.6 \mu\text{m}$  and  $w_v = 112.2 \mu\text{m}$  used to compute the integral proportional to the power  $P_0 = 2\pi I_m w_u w_v$

correcting for imperfect transmission factors. Then, from the two-dimensional Gaussian fit to the probe depicted as the contours in Figure 4.8 (magnification  $M = 5.33(10)$ ) we get  $P_0 = 143.6 \times 10^6$  counts, giving a conversion factor of  $5.76 \times 10^6$  counts/ $\mu\text{W}$ . Taking the value for  $I_{sat}$  in  $\text{mW}/\text{cm}^2$ , the demagnified pixel area  $\Delta_{pix}^2/M^2$ , and the conversion factor, we get a calibrated value  $I_{sat} = 104(15)$  counts/pixel. The drawback of this method is that the calibration compares an estimated intensity near the atoms with an intensity profile in the image plane, where the intensity is most certainly aberrated, magnified, and sometimes depleted by spurious scattering (e.g. dust, clipping apertures), causing this method to underestimate the saturation intensity value.



The second and third methods use the single photon recoil and power broadening effects respectively. The second method first demonstrated in [56], uses an orthogonal imaging system to look at the trajectory of the recoiling cloud in short time-of-flight following an imaging probe pulse. There, the displacement is limited by the saturated photon scattering rate

$$z(\delta, s_0) = z_0 + \eta \frac{\Gamma}{2} \frac{s_0}{1 + s_0 + \delta^2} \quad (4.20)$$

where  $\eta$  is the conversion from measured displacement to scattering rate. In this method, we first scan the resonant probe intensity and measure the maximum displacement

$$\delta z = \frac{\delta z_{\max}}{1 + I/I_{\text{sat}}} + \delta z_0, \quad (4.21)$$

which saturates at exactly  $I = I_{\text{sat}}$ . We demonstrate this method in Figure 4.9, where an unweighted fit to the displacement gives  $I_{\text{sat}} = 188(12)\text{counts}$ . We may use the same dataset in Figure 4.9 for the third method, where the effective linewidth

$$\Gamma = \Gamma_0 \sqrt{1 + I/I_{\text{sat}}} \quad (4.22)$$

broadens with increasing probe intensity [57]. Then, from a least squares fit to Equation 4.22, we find  $I_{\text{sat}} = 225(19)\text{counts}$ .

The fourth method uses different regimes of the corrected Beer–Lambert law, noting that the crossover between the low and high probe intensity at

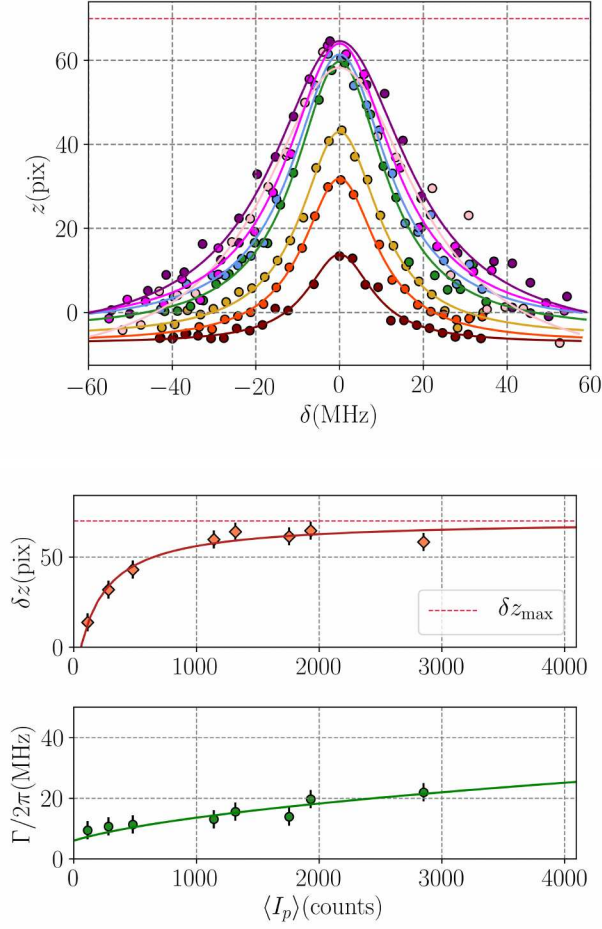


Figure 4.9: Displacement across resonance for different probe intensities at fixed  $20 \mu\text{s}$  of time-of-flight. The measured displacement (top) is proportional to the saturated scattering rate (Equation 4.20). The peak displacements (middle) give  $I = I_{\text{sat}}$  as the pulsing intensity that displaces the cloud by  $\delta z_{\max}/2$ . Additionally, power broadening lineshapes (bottom) give the saturation intensity parameter from Equation 4.22.

constant optical depth depends on the value of  $I_{\text{sat}}$ . Here, we start with the corrected optical depth

$$n\sigma_0 = -\ln\left(\frac{I_a}{I_p}\right) + \frac{I_p - I_a}{I_{\text{sat}}}, \quad (4.23)$$

from the Beer–Lambert law, where  $I_a$  represents the intensity in the presence

of atomic scatterers, and  $I_p$  represents the intensity in the absence of scatterers. In the first limit, we assume a low intensity  $I_p \ll I_{sat}$ , and low optical depth (low density)  $n\sigma_0 \ll 1$ , first allowing us to neglect the correction term so the absorbed fraction  $I_a = I_p \exp(-n\sigma_0)$ , and then linearize this relation to get  $I_a \approx I_p(1 - n\sigma_0)$ . On the other hand, in the limit of large probe intensity  $I_p \gg I_{sat}$ , at any density we see that the saturation correction term in Equation 4.23 is well in excess of the first term, allowing us to approximate  $n\sigma_0 \approx (I_p - I_a)/I_{sat}$ . Finally, a crossover regime exists when we consider very dilute clouds, such that the absorption is negligible and  $I_a \approx I_p$ . Here, we use the absorbed fraction  $I_a/I_p = 1 - \eta$  to linearize the logarithmic term  $\ln(1 - \eta) \approx -\eta$ . Then, the optical depth reads  $n\sigma_0 \approx (I_p - I_a)/I_p + (I_p - I_a)/I_{sat}$ , and the difference in counts is  $I_p - I_a \approx n\sigma_0 I_p I_{sat}/(I_p + I_{sat})$ . Table 4.1 summarizes the different approximations and the expected difference in intensities between  $I_p$  and  $I_a$ .

Low intensity, low density	High intensity, any density	Any intensity, low absorption
$I_p \ll I_{sat}, n\sigma_0 \ll 1$	$I_p \gg I_{sat}$	$I_a \approx I_p$
$I_p - I_a \approx n\sigma_0 I_p$	$I_p - I_a \approx n\sigma_0 I_{sat}$	$I_p - I_a \approx n\sigma_0 \frac{I_p I_{sat}}{I_p + I_{sat}}$

Table 4.1: Different regimes, approximations and expected difference in intensities for the corrected Beer’s law in Equation 4.23. The uncorrected Beer’s law gives an intensity difference linear in  $I_p$  while the heavily corrected Beer’s law turns the difference into a constant proportional to  $I_{sat}$ . Either regime or the full crossover model serves as a proxy for the calibration of saturation intensity.

Figure 4.10 illustrates this method. We first prepare an dilute, elongated cloud of atoms with uncorrected optical depth  $n\sigma_0 \sim 0.15$ , and we then scan the probe intensity. The linear and independent intensity difference regimes

in Figure 4.10 cross at  $I_{sat}$ , but we use the third approximation (dilute cloud) valid for all intensities to fit the data and extract the corrected optical depth  $n^*\sigma_0 = 0.436(42)$  and the saturation intensity  $I_{sat} = 226(34)$  counts/pixel. The diagonal elements of the covariance matrix from the weighed least-squares fit give the errors in the corrected optical depth and the saturation intensity, with a reduced-chi squared parameter  $\chi^2 = 2.29$  suggesting that the photon shot noise uncertainty in the mean intensity difference is insufficient, especially at high probe intensity, where saturated absorption images cause large fluctuations in  $I_p - I_a$ .

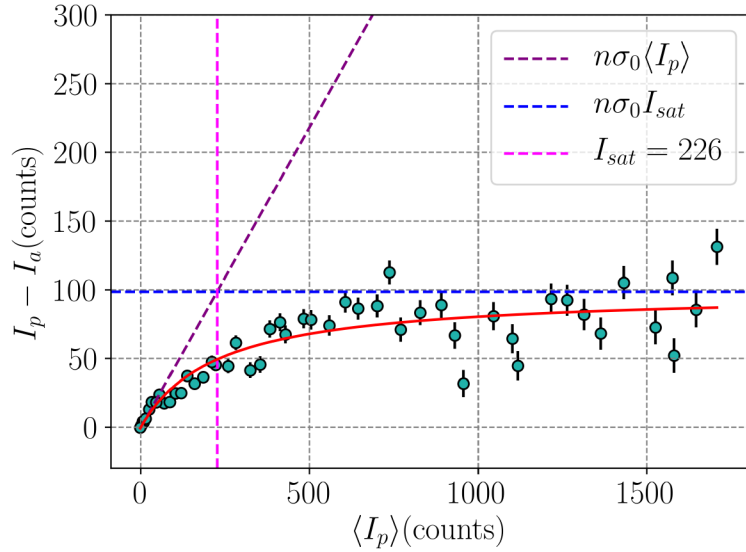


Figure 4.10: Mean difference in atoms and probe images. The crossover (dashed pink) point from the low intensity limit (dashed purple) to high intensity limit (dashed blue) assuming a dilute cloud gives the calibrated value for  $I_{sat}$ . Otherwise, the weighted least squares fit (continuous red curve) gives the correct model regardless of the density. In this measurement, we clearly identify the three regimes, and outline the calibrated value.

The final method uses the sensor specifications, and is by far the simplest requiring no atoms and a single measurement. In this method, we take a set of probe images at varying intensities and analyze the count statistics over a region with small structural probe fluctuations. In practice, since our Gaussian probes are dominated by structure, we analyze spatially lowpass filtered images at different cutoff frequencies to systematically identify their mean (from the lowpass filtered intensity), and variance (from the highpass filtered intensity). By fitting the variance with the power expansion model

$$\sigma_I^2 \approx \sigma_0^2 + \alpha \langle I_p \rangle + \beta \langle I_p \rangle^2 \quad (4.24)$$

in terms of the mean intensity  $\langle I_p \rangle$ , we extract the linear fit coefficients. Figure 4.13 shows the variance as a function of the mean detected counts in the absence of a lowpass filter, and Figure 4.13 shows the linear fit coefficients for different lowpass cutoff frequencies. We then relate these coefficients to different noise contributions. For example, the background offset coefficient tends to the technical noise baseline  $\sigma_0 \approx \sqrt{10} \text{ e}^-$ , while the background linear coefficient tends to (i.e.  $\alpha_0 = 0.239(11) \text{ counts/e}^-$ ) from the linear intercept in the right panel of Figure 6.11 (very small filter cutoffs yield low number statistics). Then, we proceed with a chain of unit conversions. First, a single  $\lambda = 780 \text{ nm}$  photon carries  $\epsilon_\gamma = 2.53 \times 10^{-19} \text{ J}$  of energy, and the transition saturates at  $I_{sat} = 6.6 \times 10^{15} \text{ photons/s cm}^2$ . Then, we use the object pixel area  $\Delta^2/M^2$ , where  $M$  is the magnification to convert into photons per second per pixel.

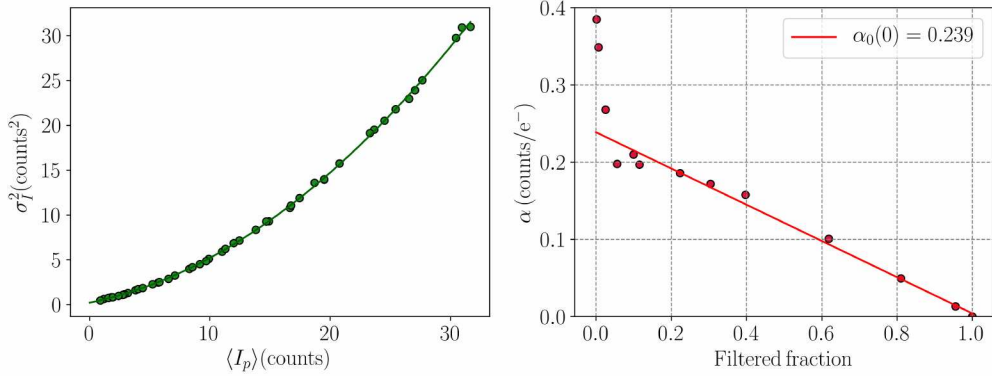


Figure 4.11: Variance calibration of  $I_{sat}$ . The photon shot noise dominated variance in the counts of the probe give the linear coefficient  $\alpha$ . In the case of a structured probe dominated by artifacts or a highly inhomogeneous intensity, we first apply a lowpass filter to all probe images and extract the mean counts. Then, we apply a highpass filter to extract the variance, which we plot against the mean in the left. We then fit the data to the model in Equation 4.24 and obtain three fit coefficients. We then repeat this procedure for different filter cutoff frequencies, and extrapolate to find the background linear coefficient  $\alpha_0$ . In the right, we show the linear coefficients as a function of filtered fraction (number of pixels within the cutoff frequency divided by total number of pixels) in the right.

Finally, we use the measured coefficient  $\alpha_0(0)$  and the pulse time to get  $I_{sat}$  in counts per pixel. For the example in Figure 4.13, we get  $I_{sat} = 122(10)$  counts assuming a quantum efficiency of 0.35 specified by the detector and a  $20\mu\text{s}$  pulse.

The different calibration methods do not overlap as we attempt them in alternating imaging systems, where the magnification, atomic clouds, and probe intensity all change. Nevertheless, Table 4.2 summarizes the different methods, the calibrated values, and their biggest drawbacks.

Method	$I_{sat}$ (counts/pixel)	Drawback(s)
Beam profile	104(15)	Typically underestimates calibration and assumes independent power measurement calibration
Recoiling cloud	188(12)	Needs two orthogonal imaging systems, and is subject to increasing Doppler shifts for long pulses [58]
Power broadening	225(19)	Requires power and frequency stabilization of the probe laser
Beer-Lambert approximations	226(34)	Needs good atom number stability and only meets two of the three approximations at low densities ( $n\sigma_0 < 1$ )
Counting statistics	122(10)	Needs careful analysis using spatial filtering on probes with structure and other artifacts

Table 4.2: Different  $I_{sat}$  calibration methods, obtained values, and method drawbacks. The different calibrations differ from each other because they represent systems with varying magnifications.

### 4.3 Image processing

This section summarizes a couple of image processing methods to obtain quantitative atomic density distributions with optimal signal-to-noise ratio. We hone these methods for the experiment in Chapter 6, but they are readily useful for absorption imaging of cold and ultracold atomic gases. The methods from the last subsection are published in [59] as a supplementary material.

We first estimate the uncertainty of the raw intensity signals in a photon shot noise limited measurement and compute the optimal signal-to-noise ratio in a measurement of linear optical depth. We then give an overview of the image reconstruction algorithms used to remove structural artifacts in the images contaminating the signal of interest.

#### 4.3.1 Estimating uncertainty

The uncertainty of a recorded intensity in a photon shot noise limited detection is described by the covariance matrix elements

$$\sigma_{ij} = \delta_{ij} \sqrt{I_i I_j}, \quad (4.25)$$

here in the pixel basis where the index  $i$  labels the  $i$ -th pixel. The uncertainty shows the uncorrelated pixel-to-pixel noise with magnitude  $\sigma_{ii}^{1/2} = \sqrt{I_i}$  at pixel  $i$ . We may propagate the uncertainty in quantities deriving from the measured



intensity using the general linear covariance transformation

$$\hat{\Sigma} = \hat{\mathcal{U}} \hat{\sigma} \hat{\mathcal{U}}^T \quad (4.26)$$

where the diagonal elements of the propagated covariance matrix  $\Sigma$  approximate the propagated error if the transformation operator  $\hat{\mathcal{U}}$  is linear. When the functional form of a derived quantity is known, we may use the regular uncorrelated error propagation. We propagate the photon shot noise limited uncertainties in the intensity from the resonant absorption images  $I_a$ ,  $I_p$ , and  $I_d$  using the corrected Beer–Lambert law from Equation 4.23. First, as  $I_d$  is a direct measurement of systematic noise, it is not limited by photon shot noise, and we subtract it directly from  $I_a$  and  $I_p$ . Then, the uncertainty in the optical depth

$$\sigma_{od} = \sqrt{\left(\frac{1}{I_p} + \frac{1}{I_{sat}}\right)^2 I_p + \left(\frac{1}{I_a} + \frac{1}{I_{sat}}\right)^2 I_a}, \quad (4.27)$$

in terms of the measured intensities and the calibrated  $I_{sat}$ .

### 4.3.2 Optimal signal-to-noise ratio

We now estimate the signal-to-noise ratio on the integrated optical depth. We consider an imperfect detector (i.e. with technical noise sources) in a perfectly dark environment, where it remains sensitive to pulsed intensities, neglecting any background light illumination. We begin by attempting the detection of a thin, elongated cloud of (linear) density  $n_0 = 10 \mu\text{m}^{-1}$ . We

assume a  $M = 5.33$  magnification imaging system, setting what fraction of the collected light is detected by a single pixel. The saturation intensity at the detector is

$$N_{sat} = I_{sat} \times Q \times \left( \frac{\tau}{\varepsilon_\gamma} \right) \times \left( \frac{\Delta}{M} \right)^2 \quad (4.28)$$

expressed as the detected number of photons per pixel, where  $Q$  is the quantum efficiency,  $I_{sat} = 1.67 \text{ mW/cm}^2$  is the saturation intensity,  $\varepsilon_\gamma = h\nu$  is the energy of a single probe photon, and  $\Delta/M$  is the effective pixel size at the object plane. Following [58], we use a  $\tau = 20 \mu\text{s}$  resonant probe pulse well within the recommended  $\tau \leq 40 \mu\text{s}$  for  $^{87}\text{Rb}$  to avoid significant Doppler shift scattering within the pulse time window. Then, we cast Equation 4.23 into

$$y + \ln \left( \frac{x}{s} \right) - s(1 - x) = 0, \quad (4.29)$$

in terms of the scattered photons  $x = N_a/N_{sat}$ , and the incident probe intensity  $s = N_p/N_{sat}$ . The optical depth is  $y = \sigma_0 n$ . Given an incident photon number  $N_p = sN_{sat}$ , and target atomic linear density  $n = y/\sigma_0$ , we numerically solve for the scattered photon number  $N_a = xN_{sat}$  and compute the detected optical depth. Then, joining photon shot noise and technical noise contributions, the uncertainties become  $\sigma_a = \sqrt{N_a + \sigma_t^2}$ , and  $\sigma_p = \sqrt{N_p + \sigma_t^2}$ . The technical noise is dominated by read noise  $\sigma_r$  and time integrated dark current background counts  $\sigma_d = j_d\tau$ , which add in quadrature. The propagated

squared uncertainty in  $y$  is

$$\sigma_y^2 = \left( \frac{\partial y}{\partial N_a} \right)^2 \sigma_a^2 + \left( \frac{\partial y}{\partial N_p} \right)^2 \sigma_p^2 \quad (4.30)$$

$$= (1+x)^2 \left( 1 + \frac{\sigma_r^2 + j_d^2 \tau^2}{N_a^2} \right) + (1+s)^2 \left( 1 + \frac{\sigma_r^2 + j_d^2 \tau^2}{N_p^2} \right) \quad (4.31)$$

where  $j_d$  is the dark current sensor specification in photons per second. The realistic SNR becomes

$$\text{SNR}_y = y/\sigma_y = \frac{s(1-x) - \ln(x/s)}{(1+x)^2 \left( 1 + \frac{\sigma_r^2 + j_d^2 \tau^2}{N_a^2} \right) + (1+s)^2 \left( 1 + \frac{\sigma_r^2 + j_d^2 \tau^2}{N_p^2} \right)} \quad (4.32)$$

with an ideal form

$$\text{SNR}_y^{(i)} = \frac{s(1-x) - \ln(x/s)}{(1+x)^2 + (1+s)^2} \quad (4.33)$$

neglecting technical noise contributions (i.e. an ideal detector), and without any kind of post-detection amplification. To compare the ideal and realistic SNR we numerically integrate the above relations as a function of  $I_p/I_{sat}$  for two different sensors. Figure 4.12 shows the side to side comparison, for two commercially available CCD cameras with and without technical noise. We highlight two qualities seen in Figure 4.12. First, the  $\sim 3$  improvement factor in maximum SNR between a “typical” and “enhanced” CCDs does not reflect a  $\sim 2$  orders of magnitude price difference. Most of the improvement seems to come from a factor of  $\sim 2$  in quantum efficiency, while the reduced dark current and readout noise by factors of  $\sim 10$  do not impact the SNR for the short imaging pulses in resonant absorption imaging. Nevertheless, commonly

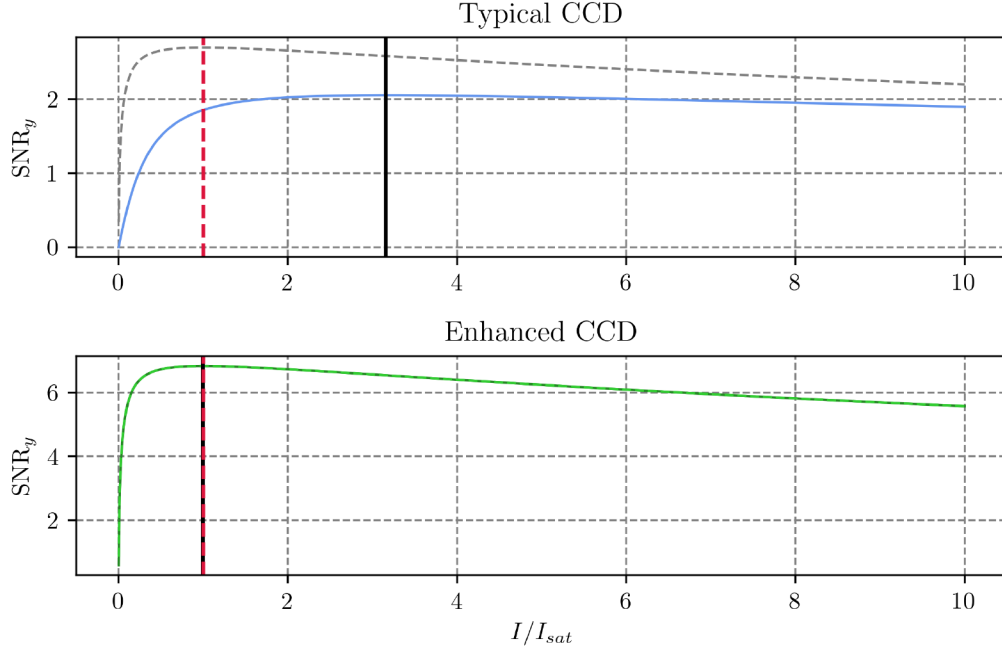


Figure 4.12: Numerically evaluated SNR for the optical depth detected in presence (dashed curve) and absence (continuous curve) of technical noise. The target (linear) density is  $n = 10 \mu\text{m}^{-1}$ , imaged with a  $\tau = 20 \mu\text{s}$  resonant probe pulse under conventional absorption imaging with a magnification of 5.33. The straight red lines show the optimal SNR intensity, while the dashed red lines show the  $I_p/I_{sat} = 1$  reference.

available sensors have tunable performance as a function of  $I/I_{sat}$ , even for the absorption imaging of extremely dilute objects. In Figure 4.13, we demonstrate this tunability by imaging a dilute, elongated cloud and estimating the signal-to-noise ratio in the integrated (linear) optical depth.

### 4.3.3 Digital processing of intensity data

We process our raw probe intensity images to remove systematic noise contributions degrading the quantitative estimate of the column and linear atomic densities. The process breaks down into several subprocesses, including probe

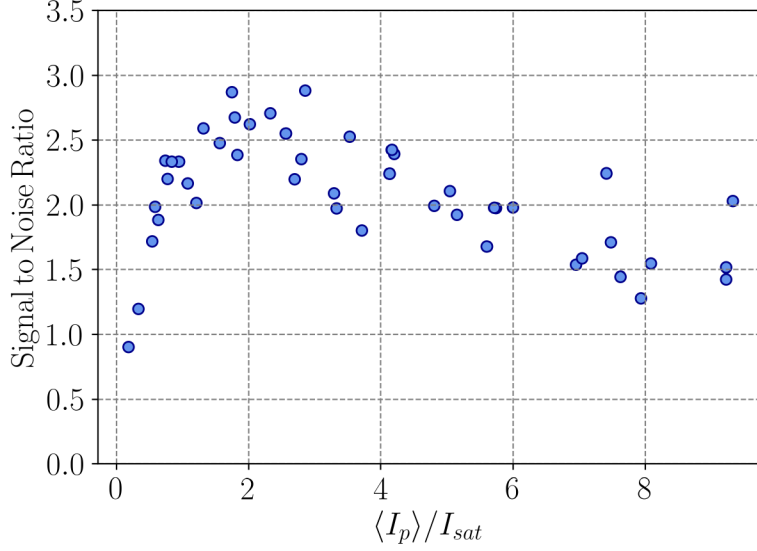


Figure 4.13: Signal-to-noise ratio in the integrated optical depth. We clearly see the optimal value of intensity of the probe maximizing the SNR. The qualitative features of the plot above agree with the models in Figure 4.12 for a typical CCD (a SONY ICX618 Mono with peak quantum efficiency of  $\sim 0.35$  at 780 nm).

image reconstruction, dark field reconstruction, dimensionality reduction for statistical averaging, and a model of linear density in the case of spatiotemporal limited detection of atomic scatterers during the probe pulse.

We perform digital probe reconstruction to interpolate an optimal probe image  $I_p^{opt}$  using an ensemble of raw probe images to construct a linear basis. The optimal probe intensity as a one dimensional vector in the pixel basis

$$\mathbf{I}_p^{opt} = \mathbb{R}\mathbf{c} \quad (4.34)$$

relates to a matrix  $\mathbb{R}$  constructed from the ensemble raw probe images as

columns and a set of scalar coefficients  $\mathbf{c}$  comprising the optimal linear combination. The optimal vector  $\mathbf{c}$  satisfies the weighted linear regression

$$\mathbb{R}^\top \mathbb{W} \mathbf{R} \mathbf{c} = \mathbb{R}^\top \mathbb{W} \mathbf{I}_a, \quad (4.35)$$

with respect to the images containing atoms  $\mathbf{I}_a$ , and where  $\mathbb{W}$  is a diagonal masking matrix of weights equal to zero for pixels containing atoms, and one elsewhere. This way, we explicitly consider only intensity fluctuations in the probe and exclude intensity fluctuations from the absorption of light by the atoms. We determine  $\mathbf{c}$  by numerically solving the linear system and construct the reshaped intensity  $I_p^{opt}$  minimizing the sum squared error with  $I_a$  in the region outside of the mask set by  $\mathbb{W}$ . The probe reconstruction is excellent to reduce the fringing artifacts due to vibrations of the imaging system between consecutive exposures. In addition, due to the dimensionality reduction from the linear regression, it reduces photon shot noise present in the reconstructed probes [60, 61]. Figure 4.14 shows the effect of probe reconstruction using  $< 100$  images as a basis.

Additionally to performing digital probe reconstruction, we correct for systematic effects in the raw dark field images. One of these effects arises from variations in ambient brightness over the line power cycle, an effect present when the CCD exposure intervals are not synchronized with the  $\sim 60$  Hz line. Another effect is stray light from imperfect extinction of laser beams (e.g.

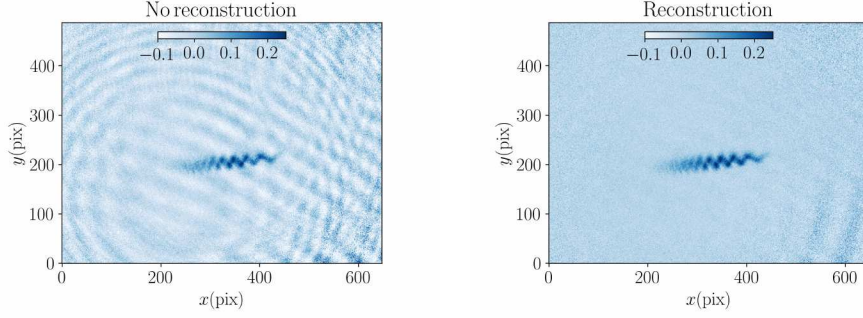


Figure 4.14: Probe reconstruction effect. Calculated optical depth for *in-situ* absorption images without reconstruction (left), and after using a 50-image reconstruction basis (right).

dipole trap beams, repump light). A last effect is structure arising from the readout pattern of the CCD. The net result is a spatially inhomogeneous difference in counts in the background light illumination. The difference in counts is small, contributing on the order of  $\approx 1$  count between  $I_a$  and  $I_p$ , but with an overall structure due to aperture, scattering, and readout effects. To correct for this effect, we fit a two-dimensional model to reconstruct the individual dark field images with a few contributions. The first one is the average dark field intensity  $\bar{\mathbf{I}}_d$  vector representing the mean dark field common to the atoms and probe images. The second contribution comes from feeding the raw dark field intensities into the probe reconstruction linear regression, giving a systematic dark field coefficient  $c_d^{sys}$  indicating how much is present in each probe image relative to the atoms image. Finally, we construct a principal component basis  $\mathbf{P}_d^{(j)}$  from the set of all dark field images, and use the first few principal components representing other sources of correlated (structured) background

illumination. The reconstructed dark field vectors

$$\mathbf{I}_d^{rec} = \bar{\mathbf{I}}_d + c_d^{sys} \mathbf{I}_d + \sum_l \mathbf{P}_d^{(l)} \quad (4.36)$$

account for the slight differences in the atoms and probe intensity dark fields.

After reconstructing the probe and dark field images, we compute the absorbed fraction

$$f = \frac{I_p^{opt} - I_a}{I_p^{opt} - I_d^{rec}} \quad (4.37)$$

in terms of the reconstructed images, as well as the calibrated saturation parameter

$$s = \frac{I_p^{opt} - I_d^{rec}}{I_{sat}} \quad (4.38)$$

in terms of the saturation intensity  $I_{sat}$  and the reconstructed images. These two quantities give rise to the naïve optical depth

$$\sigma_0^* n^* = -\alpha \log(1 - f) + sf \quad (4.39)$$

where  $\alpha = \sigma_0^*/\sigma_0$  is the empirical ratio of the two-level and effective scattering cross sections from imperfect probe polarization and/or magnetic field orientation, and  $n^*$  is a naïve column density. In reality, the naïve optical depth is not exactly accurate for systems narrower than either the optical scattering length  $\sqrt{\sigma_0/\pi} = \sqrt{3\lambda^2/2\pi^2}$ , or the imaging resolution  $\Delta x$  in at least one



direction. This is because either of these two conditions violates the assumptions behind the Beer’s law. To improve this, I later present a model of linear densities useful in the context of 1D systems violating both of these conditions.

When we compute the mean optical depth to statistically improve our SNR, we first average the absorbed fraction and saturation terms before computing the optical depth. We do so to avoid amplifying the noise baseline, an effect arising from the nonlinearity of the logarithm amplifying noisy parts of the signal fluctuating around small values. When we integrate column optical depths to produce linear cuts of the atomic density, we apply dimensional reduction of the mean absorbed fraction to mitigate the effect of the integrated photon shot noise. This process suppresses the apparent integrated absorption due to photon shot noise in regions where we know the approximate limited response of our imaging system. Here, we first crop our images to a region-of-interest containing the full extent of our imaging response function (e.g. point spread function). Then, for each position along the integration direction  $x_i$ , we extract the full linear slice of mean absorbed fraction  $\langle f(x_i, y) \rangle$  from all members of the dataset at that pixel in the central and few nearest  $m$  pixels labeled by an index  $j$ . In the pixel basis representation, we obtain the set of vectors  $\{\langle \mathbf{f}(x_{i+j}, y) \rangle\}$ . Using this large set, we perform uncentered principal component analysis [62] and extract only the first  $m$  normalized principal components to construct a dimensionally reduced absorbed fraction  $\langle f_r(x_i) \rangle$ .

The improved naïve optical depth becomes

$$\sigma_0^* \langle n_r^* \rangle \approx -\alpha \log(1 - \langle f_r \rangle) + \langle s f_r \rangle, \quad (4.40)$$

from which the average naïve linear density

$$\langle n_r^*(x) \rangle = \frac{\Delta y}{\sigma_0} \sum_y \sigma_0^* \langle n_r^*(x, y) \rangle \quad (4.41)$$

is an improved estimate of the linear density distribution.

Finally, we include a model of linear density from the column density including diffusion effects during the probe pulse. A problem for clouds with extremely narrow spatial extent in at least one dimension is that they do not just absorb light in one location of space. During the scattering process, many absorption and emission events take place, causing diffusion of the atomic wavepacket around its originally narrow confinement. This implies that we cannot infer the column density from the usual Beer's law, which assumes a stationary, extended absorber. Another consideration is the finite spatial resolution introduced by the diffraction of scattered light into our imaging system. The modified solution to Beer's law

$$\sigma_0 g(x, y, t) = -\alpha \log(1 - f(x, y, t)) + s(x, y) f(x, y, t), \quad (4.42)$$

for a column, time dependent absorbed fraction, and where  $g(x, y, t)$  represents

the column density convolved with the time-dependent atomic diffusion and spatially limited imaging resolution. The limitations imply that we have access to

$$f_m(x) = \frac{1}{\tau} \int_0^\tau \int f(x, y, t) dy \approx \Delta y \sum_y \langle f_r(x, y) \rangle, \quad (4.43)$$

in terms of the undiffracted absorbed fraction. We model the convolved column density

$$g(x, y, t) \approx \frac{n(x)}{\sqrt{2\pi\sigma_y^2(x, t)}} e^{-y^2/2\sigma_y^2(x, t)} \quad (4.44)$$

as a horizontally diffusing, vertical gaussian function. The gaussian form approximates the vertical absorption profile with unit integral (preserving the absorbed fraction), and standard deviation

$$\sigma_y^2(x, t) = \frac{\sigma_0}{\pi} + \frac{1}{3}\sigma_{v_y}^2 t^2 \quad (4.45)$$

equal to the optical scattering length  $\sqrt{\sigma_0/\pi}$  at  $t = 0$ . The momentum diffusion gives a mean squared velocity

$$\sigma_{v_y}^2(x, t) = \frac{1}{3}(2\pi)^{-1}\Gamma_s(x)v_{rec}^2 t \quad (4.46)$$

in terms of the recoil velocity  $v_{rec} = \hbar k_r/m$  and the inhomogeneously saturated, resonant scattering rate

$$\Gamma_s(x) = \frac{\Gamma}{2} \frac{s(x)}{1 + s(x)}, \quad (4.47)$$

ignoring the Doppler shifts away from resonance. Put together, the  $y$ -variance of the absorption profile

$$\sigma_y^2(x, t) = \frac{\sigma_0}{\pi} + \frac{\Gamma}{6} \frac{\hbar^2}{m^2 \sigma_0} \frac{s(x)}{1 + s(x)} t^2 \quad (4.48)$$

grows quadratically in time, approximating isotropic scattering where the change in velocity per scattering event is  $v_{rec}^2/3$ . This correction is important for higher absorbed fractions, where we find it systematically amplifies the atomic density by up to  $\approx 30\%$ .

## 4.4 Conclusion

This Chapter reviews an important set of tools that enable quantitative and precise microscopy of cold atomic ensembles. We present very simple models for imaging systems and the light-matter interaction that nevertheless capture the essential aspects of imaging cold atoms. We review the calibration methods providing guidelines for improved image processing and data analysis. We cover the propagation of uncertainty, and analyze the optimized signal-to-noise ratio in absorption imaging, which are essential in the absolute determination of column densities. Lastly, the image processing algorithms remove systematic contributions from the environment and the detection process. Some of the methods in this Chapter, including the probe reconstruction, dark frame reconstruction, and the modelled linear absorption are published in [59] as a supplementary material.